J. Fluid Mech. (1998), *vol.* 363, *pp.* 173–198. Printed in the United Kingdom

Shock oscillation in underexpanded screeching jets

By J. PANDA

Modern Technologies Corporation, Middleburg Heights, OH 44130, USA *and* NASA Lewis Research Center, Cleveland, OH 44135, USA

(Received 23 July 1996 and in revised form 12 December 1997)

The periodic oscillation of the shock waves in screeching, underexpanded, supersonic jets, issuing from a choked, axisymmetric, nozzle at fully expanded Mach numbers (M_j) of 1.19 and 1.42, is studied experimentally and analytically. The experimental part uses schlieren photography and a new shock detection technique which depends on a recently observed phenomenon of laser light scattering by shock waves. A narrow laser beam is traversed from point to point in the flow field and the appearance of the scattered light is sensed by a photomultiplier tube (PMT). The time-averaged and phase-averaged statistics of the PMT data provide significant insight into the shock motion. It is found that the shocks move the most in the jet core and the least in the shear layer. This is opposite to the intuitive expectation of a larger-amplitude shock motion in the shear layer where organized vortices interact with the shock. The mode of shock motion is the same as that of the emitted screech tone. The instantaneous profiles of the first four shocks over an oscillation cycle were constructed through a detailed phase averaged measurement. Such data show a splitting of each shock (except for the first one) into two weaker ones through a 'moving staircase-like' motion. During a cycle of motion the downstream shock progressively fades away while a new shock appears upstream. Spark schlieren photographs demonstrate that a periodic convection of large organized vortices over the shock train results in the above described behaviour. An analytical formulation is constructed to determine the self-excitation of the jet column by the screech sound. The screech waves, while propagating over the jet column, add a periodic pressure fluctuation to the ambient level, which in turn perturbs the pressure distribution inside the jet. The oscillation amplitude of the first shock predicted from this linear analysis shows reasonable agreement with the measured data. Additional reasons for shock oscillation, such as a periodic perturbation of the shock formation mechanism owing to the passage of the organized structures, are also discussed.

1. Introduction

The flow field of incorrectly expanded jets is characterized by a train of shock waves, which upon interacting with the jet turbulence, produce 'shock-associated noise'. Under a special self-resonance condition, first outlined by Powell (1953), incorrectly expanded jets emit very intense pure tones, known as screech. Owing to its primarily upstream directivity, the intense screech tones are capable of causing structural damage and fatigue failure of airplane components (Hay & Rose 1970; Seiner, Manning & Ponton 1987). The ultimate motivation served by the current work is to provide a knowledge base and a database which can be used along with computational methods (Cain *et al.* 1995) to predict the frequency and amplitude of the screech tone.

Since the earlier work of Powell (1953) and Harper-Bourne & Fisher (1974), screech (and in general 'shock-associated noise') has been associated with the oscillation of the

shock system formed inside a supersonic jet. Although a large amount of research effort has been devoted to the measurement and analysis of the acoustic field, very little is known about the oscillation of the shock cells. In a review article on jet noise, Seiner (1984) expressed his surprise at the lack of information on shock motion, which is necessary to model screech. This has delineated the goal for the present experimental work. Currently, an experimental program is being undertaken at the NASA Lewis Research Center to explore various aspects of screech noise. The present paper reports the unsteady motion of various shocks measured using a new shock-detection technique. An accompanying work that describes the acoustic field generated by the identical jets can be found in Panda (1996).

The flow fields of underexpanded jets are not well understood. So far, the primary sources of experimental data are schlieren photographs, and the analytical solutions are available for linearized descriptions. The earliest analytical expression is the Prandtl–Pack relation (Pack 1950). The success of the small perturbation, linearized Euler's equation solution, with the vortex sheet boundary condition, is primarily limited to a reasonable prediction of shock-cell spacing. The vortex sheet model was extended to predict shock-cell spacing in a non-circular jet by Tam (1988) and Morris, Bhat & Chen (1989). Tam & Jackson (1985) solved an Orr–Sommerfield equation using multiple-scale expansions and showed the propagation of various waveguide modes forming expansion and compression fans that are trapped as shock cells. It should be pointed out that the linearized models do not allow for any shock formation; the flow field is composed of expansion and compression waves only. In reality, schlieren photographs (see Johannesen 1957; Love *et al.* 1959) show that shock waves are formed in an underexpanded jet. The linearized description is also used in the shock-noise models of Howe & Ffowcs Williams (1978) and Tam (1972). Perhaps the need for the linearization is a simplification of the nonlinear Euler's equation, rather than providing an exact description of the jet flow. The shock formation mechanism is the subject of Pack (1948), where the flow fields of underexpanded jets are calculated by the method of characteristics and the shock formation is explained as a merging process of the compression waves. The wave structures inside a shock cell are quite complex and for low levels of underexpansion weak shocks are formed. The shock strength increases with an increase of the degree of underexpansion. Johannesen & Meyer (1950) and Love *et al.* (1959) describe the same mechanism for the inception of a shock.

From the noise generation point of view, the interest is in the unsteady shock motion resulting from an interaction with the shear layer turbulence. The earlier analytical model of homogeneous turbulence interacting with a single shock (Ribner 1969), and the recent computations of single vortex and single shock interactions (Ellzey *et al.* 1995; Meadows & Caughey 1996), demonstrated the generation of vorticity, entropy and sound waves as well as distortions of the shock surface. These results, however, are not directly applicable to a jet flow field, where a train of shock waves interact with a series of coherent vortices. In addition, a screeching jet represents a special situation where the sound waves, created from the shock–turbulence interaction, propagate along the outskirts of the jet boundary (Panda 1996). In effect, the pressure fluctuations associated with the screech tone perturb the quiescent surrounding into which the jet flows. An analytical calculation, based on the linear theory of shock formation, is presented in this paper which shows the influence of this fluctuation in generating disturbances in the jet column and contribution to the shock oscillation. Various other interactions relating coherent vortical structures and the nonlinear shock formation mechanism are qualitatively discussed.

Experimentally, the oscillation of the shock waves at the screech frequency was observed first by Lassiter & Hubbard (1954) through a shadowgraph image of a shock cell. The shock-noise theory of Harper-Bourne & Fisher (1974) was based upon the experimental observation that the shock oscillation is well correlated with the broadband noise component. Westley & Woolley (1968*a*, *b*, 1970) are of particular interest. Some features of shock oscillation, quantitatively measured in the present work, have been qualitatively described through schlieren visualization in these references.

The primary experimental tool, which has made the present investigation possible, is an optical shock detection technique that depends on laser light scattering by shock waves. The fundamental optical property of a shock wave, which is exploited in the detection technique, has been observed recently (Panda 1995*a*, *b*; Panda & Adamovsky 1995). A brief discussion of the optical property follows. When a narrow laser beam is brought to a grazing incidence on a shock, scattered light is found to appear from the point of interaction. The scattered light, when visualized on a screen, appears as a long streak oriented normal to the shock surface. It disappears when the beam is moved to any other location where there is no shock or when the beam pierces the shock surface at a non-grazing incidence. The phenomenon is due to light diffraction caused by a sudden jump in the refractive index across a shock. At a grazing incidence a part of the beam propagates upstream of the shock (lower density, lower refractive index) and the rest downstream (higher density, higher refractive index). The refractive index difference produces an optical path difference between these two parts of the beam, which ultimately results in wide-angle scattering. The intensity of the scattered light is found to increase exponentially as the difference of fluid density (refractive index) increases.

The central element of the shock detection technique is a narrow laser beam which is moved from point to point in a flow field containing shocks, and the appearance of the scattered light is sensed using a photomultiplier tube (PMT). The beam locations which correspond to the non-zero PMT signal are the shock locations. Further details of the shock detection technique will be given in the next section describing the experimental set-up.

2. Experimental set-up

2.1. *The optical device*

Figure 1(*a*) shows the optical set-up. A green (0.514 μm wavelength) laser beam, separated from an Argon–ion laser and transmitted through a fibre optic system, is used for the measurement. The 2 mm diameter laser beam coming out of the fibre optic probe is focused to a 0.16 mm spot at the jet centreline and is allowed to cross the shock-containing plume. On the other side of the jet there is a light-collecting and measuring device which senses the scattered light. There is a beam stop and an aperture stop just in front of the 60 mm diameter collecting lens. The diameter of the beam stop is such that the main laser beam is blocked from entering the collecting optics, while the wide-angle scattered light can be easily collected. For the present experiment, beam stops of 19 mm and 12.5 mm diameters were used. The distance between the jet centreline and the collecting lens is the focal length of the latter, 250 mm. The collecting lens focuses this light to a 0.2 mm diameter pinhole which then passes it to a PMT. The electrical output from the PMT is connected across a 50 ohm terminator. The voltage drop across the terminator is proportional to the PMT current and, therefore, is an indicator of the intensity of the collected light.

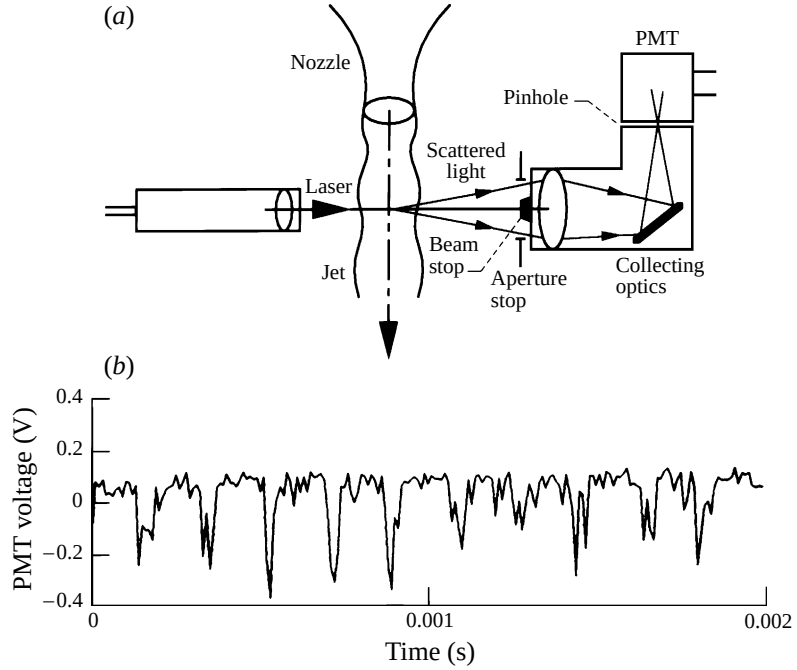

FIGURE 1. (*a*) Schematic of the shock detection technique. (*b*) Signal from photomultiplier tube when the laser beam touches the oscillating first shock in $M_j = 1.4$ jet at $r/D = 0$.

The depth of field of the optical system is controlled by the *f*-number of the collecting lens and the diameters of the beam stop, aperture stop and pinhole. For the present combination, the collection efficiency is found to be reduced by 90% if the scattered light appears ± 4 mm ($\pm 0.15\ r/D$) away from the focal plane.

The diameter of the beam stop is found to control the noise level of the PMT signal. The random refractive index fluctuation caused by turbulence in the shear layer produces weak scattering close to the beam. As the beam stop diameter is reduced, more and more of this scattered light is collected which then appears as random noise in the PMT signal. However, the noise level was two to three orders of magnitude lower than the level produced by the intense scattering from the shock–laser interaction.

The complete optical set-up (fibre optic probe, beam stop and the collecting optics) was mounted on a 3-axis traversing unit which allowed it to be moved along the streamwise and the transverse directions within an accuracy of 0.025 mm. Under normal circumstances light from the laser beam does not reach the PMT. However, if the laser beam touches a shock surface in the focused plane, a part of the scattered light is collected and sensed by the PMT which then produces a non-zero output. The voltage signal from the PMT and all other voltage outputs from various measuring devices were digitized using a sample-and-hold digital converter and then stored and processed by a Microvax 3300 computer.

Figure 1(*b*) shows a time trace obtained from the PMT when the laser beam was placed to just graze the first shock in an underexpanded jet of Mach number 1.4. The shock was unsteady and was oscillating at the screech frequency of about 5.5 kHz. The nearly periodic negative spikes at this frequency indicate that the scattered light appears and disappears periodically as the oscillating shock intercepts the laser beam. The availability of an electrical signal, similar to that of figure 1(*b*), which is indicative of a shock surface grazing the laser path is the basis of the detection technique.

2.2. *Facility and test conditions*

The present experiments were conducted in a free air jet facility at the NASA Lewis Research Center (Panda 1996). A 25.4 mm diameter (D) axisymmetric, convergent nozzle is used to produce underexpanded supersonic jets, which, if fully expanded would have Mach numbers (M_j) in the range from 1.1 to 1.65. The Mach number range was achieved by changing the supply pressure to the plenum chamber.

During the detailed shock profile survey, it was observed that the circumferential symmetry of the shocks is extremely sensitive to the symmetry of the flow field. Any small asymmetry in the flow, introduced by a small misalignment or by an asymmetric blockage in the plenum chamber, causes detectable asymmetry in the shock structure and, sometimes, the appearance of an additional weak shock system on one side of the jet. Therefore, special care had to be taken to eliminate all sources of asymmetry from the jet facility.

One undesirable feature, when making phase-averaged measurements, is the unstable nature of the screech tone (Davis & Oldfield 1962) for most of the operating (M_j) conditions. The microphone signal shows that the screech appears in bursts, which become more intermittent during mode switching. Since the oscillation of the shocks is found to be closely tied to the nature of the screech tone, it was necessary to operate the jet at a few selective Mach numbers where stable tones can be obtained over a long period of time. The detailed data were taken for two operating conditions, for which the fully expanded jet Mach numbers (M_j), screech frequencies and screech modes are, respectively, 1.19, 8400 Hz, axisymmetric, and, 1.42, 5400 Hz, helical. The corresponding Reynolds numbers, based on the fully expanded jet velocity, U_j, and the nozzle diameter are, respectively, 0.93×10^6 and 1.2×10^6.

Another concern, that finally limits the measurement accuracy, is the fluctuating plenum pressure which also moves the shock structures. The compressed air was supplied from a central facility which feeds many other test installations. Therefore, certain fluctuations were unavoidable. However, the plenum pressure, measured using a pressure transducer, was continuously monitored and the data acquisition was performed only when it remained within $\pm 0.7\%$ of the desired setting. This condition was imposed for all data presented in this paper.

The flow field was visualized by a standard schlieren system using two 152 mm diameter and 914 mm focal length spherical mirrors. The details of the schlieren system can be found elsewhere (Panda 1996). A limited amount of time-averaged axial velocity data obtained from a 1-component, dual-beam, forward scatter, LDV system are presented. The system consists of a 4 watt, Lexel, argon-ion laser as the light source, a TSI Colorburst unit (TSI 9201) for colour separation and beam splitting purposes, fibre optic cables and a two-component fibre optic probe (TSI 9118). To minimize the particle lag in the shock-containing plume, very small diameter (0.6 μm) polystyrene latex (PSL) spheres were used as seed particles.

3. Results and discussion

3.1. *Visualization of the motion*

Figure 2 shows time-averaged and instantaneous schlieren visualizations of the jet flow field. Flow is from left to right in all photographs presented in this paper. The time-averaged photograph was obtained by exposing a single negative to eight random flashes. The darker regions of figure 2(*a*) represent shock compression and the brighter ones expansion zones. The sharp vertical boundaries at the end of each compression

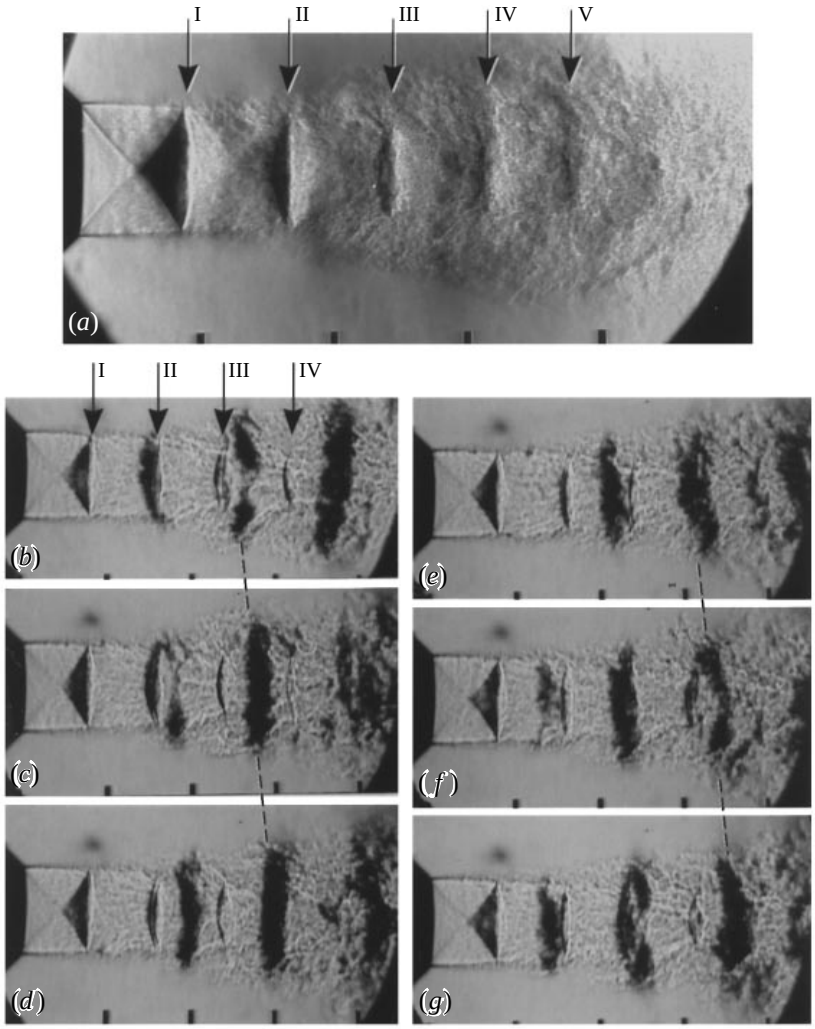

FIGURE 2. Schlieren photographs of $M_j = 1.19$ jet. (*a*) Time-averaged photograph; (*b*)–(*g*) spark schlieren photographs at equal phase intervals over a screech cycle. The vertical arrows denote shock locations. The dashed line joins the positions of one organized structure.

zone correspond to the termination position of each shock in the shear layer. Such termination positions are marked by vertical arrows, and numbered by Roman numerals beginning with the first shock from the nozzle exit.

The spark schlieren photographs of figures 2(*b*) to 2(*g*) are significantly different from the time-averaged one. In addition to the shock compression regions, there are dark axisymmetric structures that convect downstream as the phase time progresses. A chain line, joining the positions of one such structure, shows the convection process. These are identified as the organized turbulent vortices convecting downstream with the flow. Recall that the screech mode for the $M_j = 1.19$ jet is axisymmetric; therefore, the organized turbulent vortices are also axisymmetric. The 1 microsecond spark duration has essentially frozen the flow at various phases of screech cycle, and has made the convective structures visible; while the random exposures of the time-averaged photograph have averaged out their footprints. The shock waves, especially

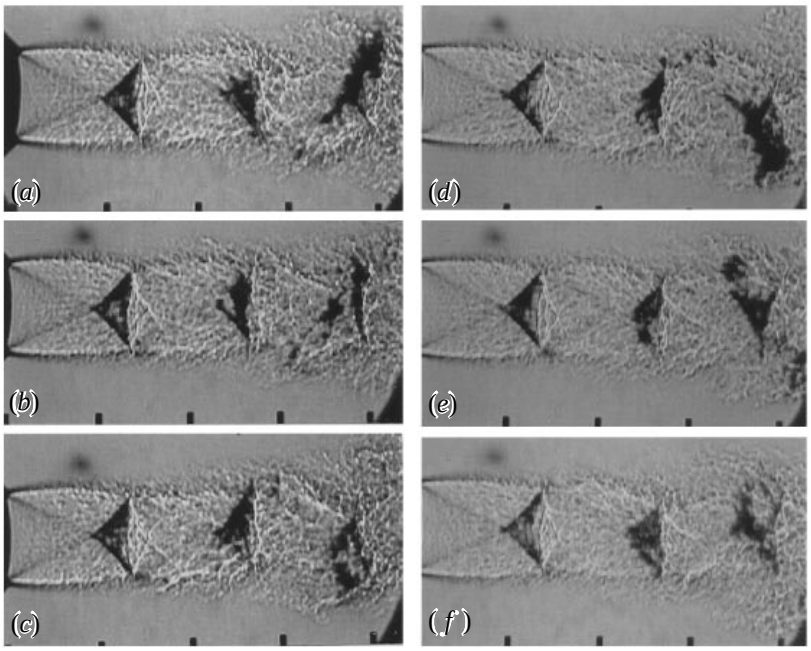

FIGURE 3. Spark schlieren visualization of $M_j = 1.42$ jet at equal phase intervals over a screech cycle.

the ones lying further downstream from the nozzle exit, undergo considerable distortion and show some oscillation.

The shock oscillations are somewhat clearer in figure 3, which shows the $M_j = 1.42$ jet. A lower schlieren sensitivity, obtained from a lower knife-edge cut off, has eliminated the impressions of the large organized vortices, while leaving behind the signatures of the strongest density gradients present across the shocks. Similar to the preceding figure, the distortion and displacement progressively increase for the shocks formed further downstream from the nozzle exit. The first shock does not show any discernable motion. A careful examination of the individual shock boundaries from frame to frame shows a vertical up and down motion and associated deformation of the triangular shape of the second and third shocks. These are two-dimensional impressions of a helical motion where the shock cones precess about the jet centreline. Note that the screech mode for this Mach number condition is also helical. Further details of the shock motion will be clear from the quantitative data.

In this context two excellent ciné films of schlieren visualization by Westley & Woolley (1968*a*, 1970) should be mentioned. (These were brought to the author's attention after completion of the present work.) The shock–turbulence interaction visualized in these films shows generation of a new shock when a turbulent disturbance convects over an existing shock wave. This has been referred to as shock splitting in this paper. The second shock of figure 2(*d*) and the third shock of figure 2 (*b*) indicate the shock splitting phenomenon. Since, a schlieren photograph presents integrated information over the light path from shock waves, turbulent eddies and sound waves, definite conclusions about shock oscillation cannot be made. This is overcome by the laser scattering technique which has a short depth of field, and a strong scattering signature clearly differentiates shock splitting from all others.

3.2. *Time-averaged measurement*

The optical detection technique provides an easy tool to measure quantitatively the position of the shock waves and the distance over which they move. The time-averaged shock position is determined by moving the laser beam from point to point along the streamwise direction and by measuring the root-mean-square (r.m.s $\sqrt{V^2}$) value of the voltage drop (V) across the photomultiplier tube. It is worth repeating here that the r.m.s. reading from the PMT circuit is zero if there is no shock on the laser path, or if the laser is piercing the shock without being tangent to any part of it. However, if the beam is touching a shock surface, a large r.m.s. reading is obtained. Figures 4(*b*), 4(*c*) and 4(*d*) show results of axial traverses from three radial positions; $r/D = 0.4$, 0.2 and 0 (centreline), respectively.

The time-averaged schlieren photograph of the $M_j = 1.4$ jet in figure 4(*a*) shows the shock locations. The shock position data obtained by a laser survey close to the shear layer ($r/D = 0.4$, figure 4*b*) are characterized by quasi-periodic spikes which line-up with the base of the triangular shock boundaries seen in the schlieren photograph. Similar data obtained from inside the jet ($r/D = 0.2$ and 0, figures 4(*c*) and 4(*d*)) show that the spikes appear progressively upstream. This is consistent with the conical shape of the shock surfaces. For example, the narrow laser beam touches a shock cone at points further upstream when traversed along the jet centreline ($r/D = 0$) as compared to a similar traverse made at $r/D = 0.2$. The height of each spike is related to the scattered light intensity, which, in turn, is related to the shock strength. As the density jump across a shock increases the scattered light intensity also increases. The relationship, however, is very nonlinear (Panda & Adamovsky 1995). Moreover, for oscillating shocks the measured voltage depends on the fraction of time the shock surface is in position to scatter the light beam. Therefore, it is difficult to draw any quantitative inference about shock strength from the absolute value of the photomultiplier signal. Nevertheless, in a qualitative sense, based on the progressive drop in the r.m.s. voltage peak, it is expected that the shock strength progressively diminishes from the first to the fourth shock. Noticeably, the r.m.s. voltage obtained from the centreline position of the second shock (figure 4*d*) is very weak. A possible reason for this is discussed in the next section where phase-averaged measurements are presented. Such measurements are also useful in explaining another feature: an increase in the width of the r.m.s. voltage spikes (for all but the first shock) from the shear layer to the centre of the jet. The width shows the spatial distance over which a particular shock can be detected, and is a measure of the amplitude of shock oscillation.

The shock position data shown in figures 4(*b*) to 4(*d*) are affected by the depth of field of the optical set-up. The experimental set-up used for the earlier data, presented in Panda (1995*b*) had a very large depth of field that sensed scattered light generated anywhere on the laser path. Therefore, similar time-averaged shock position data presented in the above reference are more complex to analyse. It has been mentioned above that the depth of field of the current set-up is ± 4 mm ($\pm 0.15\ r/D$).

The Mach number distribution of figure 4(*e*) was obtained by laser-Doppler velocimetry (LDV) measurements of the time-averaged axial velocity component. The distribution shows many undulations with the local value overshooting the fully expanded jet Mach number and then smoothly dropping close to unity. The dashed lines between figures 4(*d*) and 4(*e*) mark the upstream extreme of motion of each shock. It can be seen that, in general, local Mach number increases up to this boundary and then starts to drop. Unlike a sharp drop expected across a stationary shock, the

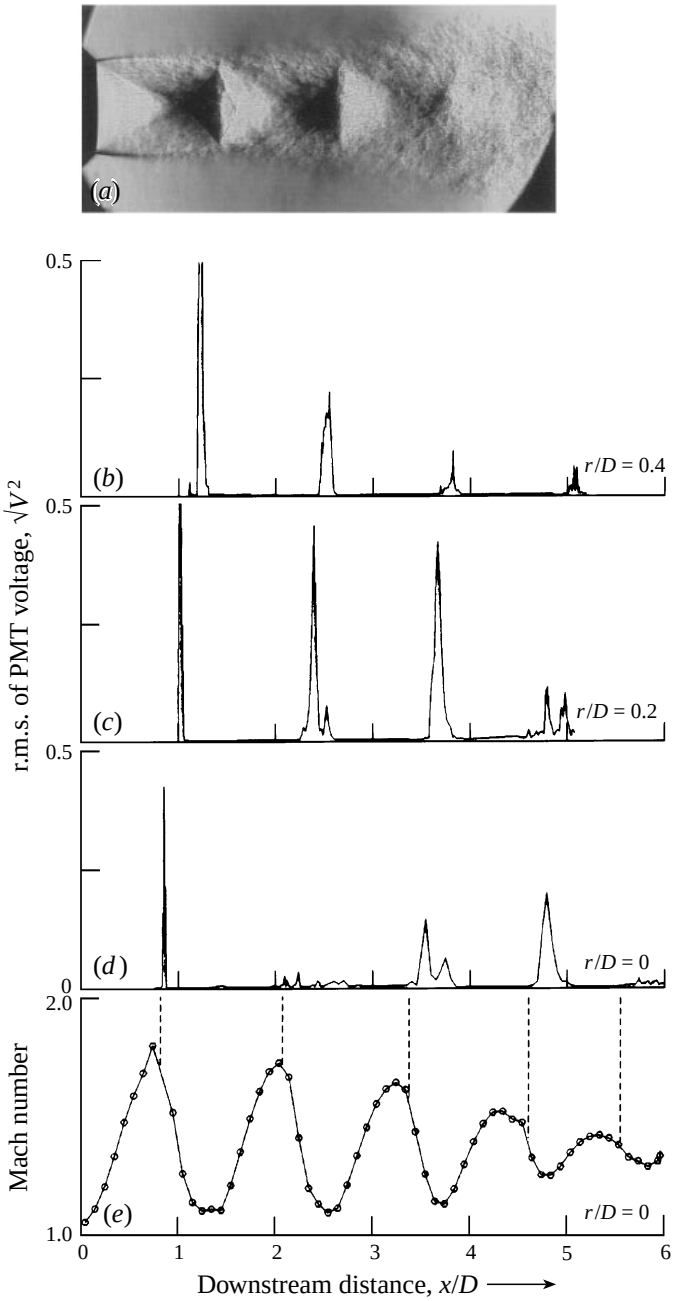

FIGURE 4. (*a*) Schlieren photograph of $M_j = 1.42$ jet; (*b*)–(*d*) Shock locations identified by laser survey from indicated radial positions; (*e*) Centreline Mach number distribution obtained from LDV measurement.

measured decrease is far too smooth. Velocity measurements across a shock are always affected by 'particle lag', that is, the inability of the particles to decelerate to the downstream velocity after crossing a shock. The required distance needed to attain 95% of the downstream velocity, for the present condition, is estimated to be about 2 mm ($x/D = 0.08$, Vom Stein & Pfeifer 1972; Yanta, Gates & Brown 1971). However,

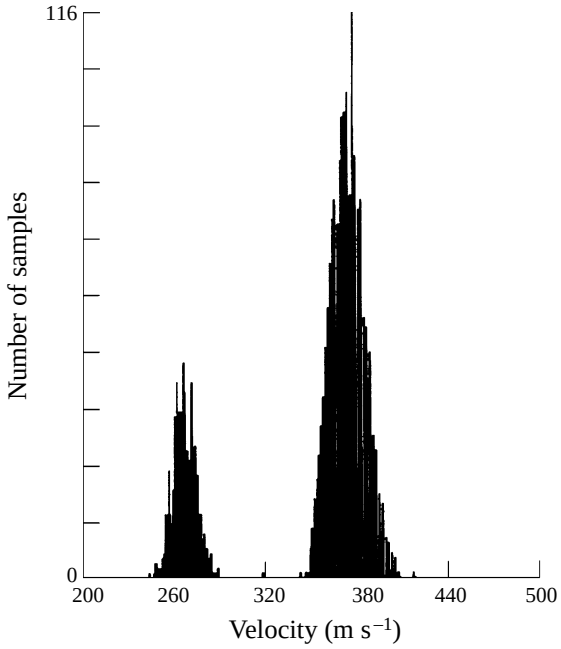

FIGURE 5. Histogram of the particle velocity distribution in $M_j = 1.42$ jet at $x/D = 2.37$, $r/D = 0$.

the measured data of figure 4(*e*) show that the velocity distribution drops slowly over an average distance of 15 mm, half of the shock cell spacing. It is believed that there are two reasons for the slow decrease. First, it is due partly to the compression fan that exists beyond the oblique shock boundary (Pack 1948). Secondly, the shock motion plays a significant role in smoothing out the velocity variation. Additional evidence is provided in figure 5 which shows the histogram of the particle velocity distribution obtained from the second shock location. This histogram is bimodal with a high (average of 372 m s^{-1}) and a low (average of 267 m s^{-1}) velocity mode. As the shock oscillated back and forth about the measurement point, particles moving at a speed of either the upstream or the downstream side of the shock were encountered, leading to the bimodal distribution. Such bimodal histograms were also reported earlier in the literature on LDV measurements around an oscillating normal shock (Chriss 1991). In the present experiment, such distributions were obtained from many measurement stations lying in the shock oscillation regions. Clearly, the time-averaged measurement masks such details and provides a smoother velocity distribution which is very different from the instantaneous picture.

One particular problem in LDV measurements in the vicinity of a shock, is the appearance of the shock–laser interaction phenomenon when any of the two beams becomes tangent to the shock surface. In other words, the phenomenon of light scattering by the shock waves, the basis of the present shock-detection technique, also appears undesirably during LDV measurements. The data rate is found to change unpredictably in these regions. The effect of this phenomenon on the LDV data has remained unclear.

3.3. *Phase-averaged measurements*

The time-averaged laser survey data, presented earlier, provide only the locations where shock waves are present. To determine the unsteady characteristics of the shock motion, phase-averaged measurements were performed. Since the shocks oscillate at

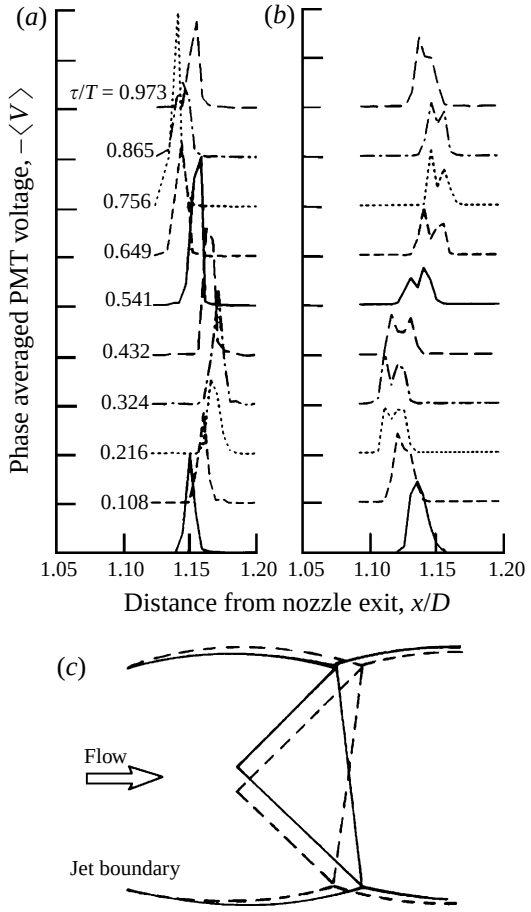

FIGURE 6. Phase-averaged PMT data at indicated phases of screech cycle showing the motion of first shock in $M_j = 1.42$ jet at (*a*) $r/D = 0.3$ and (*b*) $r/D = -0.3$. (*c*) A schematic of oscillation.

the screech frequency, the signal from a microphone placed upstream of the nozzle is used as a reference for the phase-averaged measurements. To eliminate the harmonics and other noise components, the reference microphone signal is band-pass filtered about the fundamental screech frequency. This produces a repeatable phase reference. The optical system is traversed from point to point in the flow field and, at every point the PMT signal, $V\{t, x/D, r/D\}$, is phase averaged over more than 100 screech cycles to obtain $\langle V\rangle\{\tau/T, x/D, r/D\}$. The data are stored in the Microvax computer for later processing.

To determine the instantaneous axial position of a shock at a given radial distance (r/D), the phase-averaged voltage values are retrieved for all streamwise locations (x/D). Figures 6(*a*) and 6(*b*) show two such plots, for 10 different phase times, τ/T, for the first shock in the $M_j = 1.42$ jet. Since the amplitude of motion of this shock is very small (about 1.25 mm), only a short streamwise distance is shown in each figure. Note that there are more than 20 data points, at an interval of 0.127 mm, used in each plot. Such a fine resolution was possible owing to the small laser beam waist (0.16 mm) used in the experimental technique. The single peak showing the position of the shock is seen to oscillate sinusoidally. In figure 6(*a*), the shock at first moves downstream to its extreme position and then returns back to its upstream extreme. However, in figure

6(*b*), corresponding to a diametrically opposite radial station, the shock motion is reversed, that is 180° out of phase. Various information, such as the amplitude and the mode shape of shock motion, can be obtained from data similar to those shown in figures 6(*a*) and 6(*b*). The oscillation amplitude is the streamwise distance between the extreme positions of the shock. Further discussion of the oscillation amplitude is postponed to a later part of the text. A discussion of the mode shape of shock motion follows.

Determination of the circumferential mode of oscillation requires measurement of the relative phase at a few circumferential locations. The traversing unit on which the optical detection system was mounted, however, did not allow circumferential rotation of the laser beam. Measurements could be made at different radial positions over a meridian plane. It is observed that the phase-averaged PMT traces obtained from the first shock are identical to that shown in figure 6(*a*) for all radial locations above the jet centreline ($r/D > 0$), and to that of figure 6(*b*) for all locations below the jet centreline ($r/D < 0$). In other words, the complete upper leg oscillates in phase and the same is true for the lower leg, while a phase difference of 180° is maintained between them. A schematic of the motion is shown in figure 6(*c*). The triangular shock boundary is shown to tilt forward and backward. Some supporting evidence for such a motion can be found in the flow visualization photographs of figure 3. Such a tilting motion in the plane of measurement can be due to a helical or a flapping mode, and more data at a few other circumferential locations are necessary to determine the exact mode of oscillation. However, in view of the helical mode of the screech tone emitted by the $M_j = 1.42$ jet, it may be concluded that the shock cone also oscillates in a helical fashion.

Data presented in figures 6(*a*) and 6(*b*) show a smooth sinusoidal motion, which is found to be characteristic of the first shock in all underexpanded jets studied for the present experiment. The motion of the subsequent shocks, however, is found to be more complex and involves the universal feature of a sudden splitting into two shocks. This is demonstrated in figure 7 where the instantaneous profiles of the third shock in the $M_j = 1.19$ jet are presented. The phase-averaged PMT data for a given phase of the screech cycle, obtained from traverses at nine different radial stations, are plotted in the individual graphs. Out of 23 such graphs covering a screech cycle, only six are shown in figure 7. Data from each axial traverse is shifted vertically by its radial position (see the graph for $\tau/T = 0.347$), and the spatial distance covered in both abscissa and ordinate is the same: one jet diameter. There are 20 to 40 data points in each axial traverse and the total distance covered in each traverse was carefully chosen to cover the complete amplitude of shock motion. Determination of the shock shape from such a multiple plot of the phase averaged PMT data is shown in the graph for $\tau/T = 0$. Since, in any axial traverse the *base position* of the voltage peak represents the shock location, such positions in each trace are marked, and a smooth line is drawn through all such marks. This smooth line represents the shock front at the particular phase of the screech cycle.

The shock fronts seen in figure 7 appears to have the shape of a concave disk (as opposed to a cone) in three dimensions. This is supported by the appearance of the same third shock in the schlieren photograph of figure 2(*a*). The shock also moves in an axisymmetric mode which is consistent with the screech mode radiated by the jet. As the phase time τ/T progresses from 0, the centre of the shock moves downstream (i.e. the concaveness decreases). At the phase time of 0.347, a second weak shock appears upstream, which progressively becomes stronger and also moves downstream. Meanwhile, the original shock, still moving downstream, becomes weaker and is seen

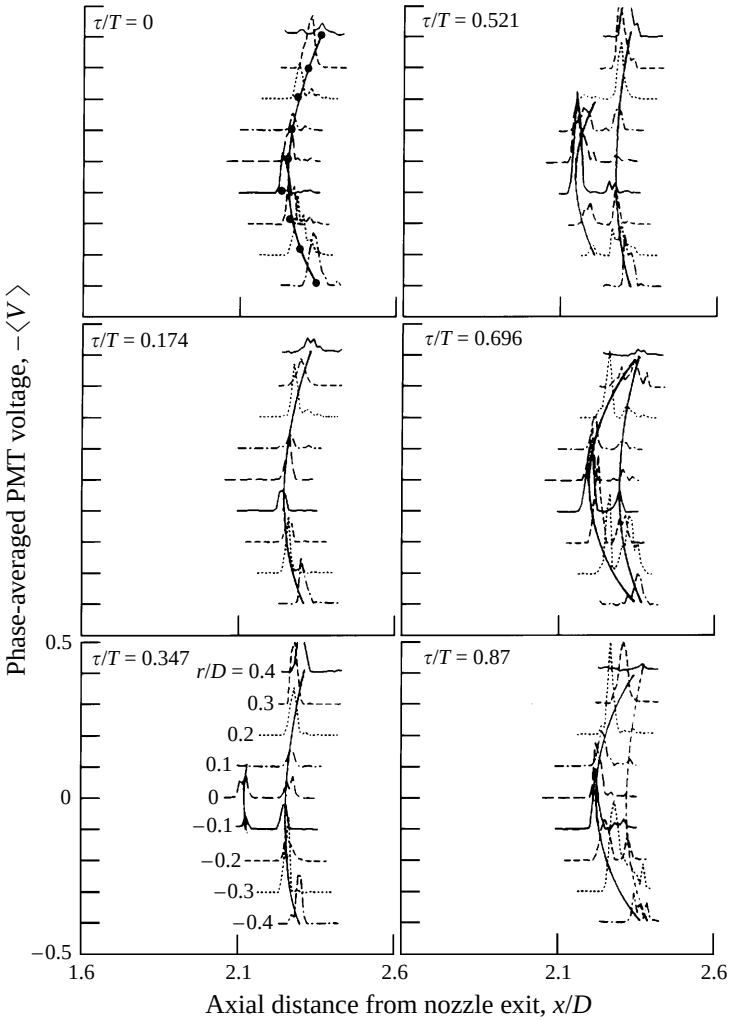

FIGURE 7. Phase-averaged PMT data obtained at nine different radial stations arranged to show the instantaneous profiles of the third shock at the indicated phases of the screech cycle.

to disappear at $\tau/T > 0.87$. The process repeats at each screech cycle, which makes the shock motion analogous to that of a moving staircase.

To visualize the relative motion between the neighbouring shocks, data similar to figure 7 obtained for the first four shocks formed in the $M_j = 1.19$ jet are presented in figure 8. The phase reference for all measurements was obtained from a single microphone placed at a fixed location upstream of the nozzle exit. To construct this figure individual graphs showing the instantaneous positions of each shock are plotted. Subsequently, all such plots for a given phase of the screech cycle are pasted together. Note that the spacings between the shocks shown in this figure are not the true spacings, as individual graphs are pasted closer to save space.

The first shock has an unexpected diamond shape. The upstream part of the diamond is due to the conical first shock (see schlieren photograph of figure 2*a*). However, the additional downstream part may be due either to a reflection of the upstream shock from the shear layer, or to a slip stream which may be able to cause laser light scattering. The combined system moves by a far smaller amplitude (fraction of a

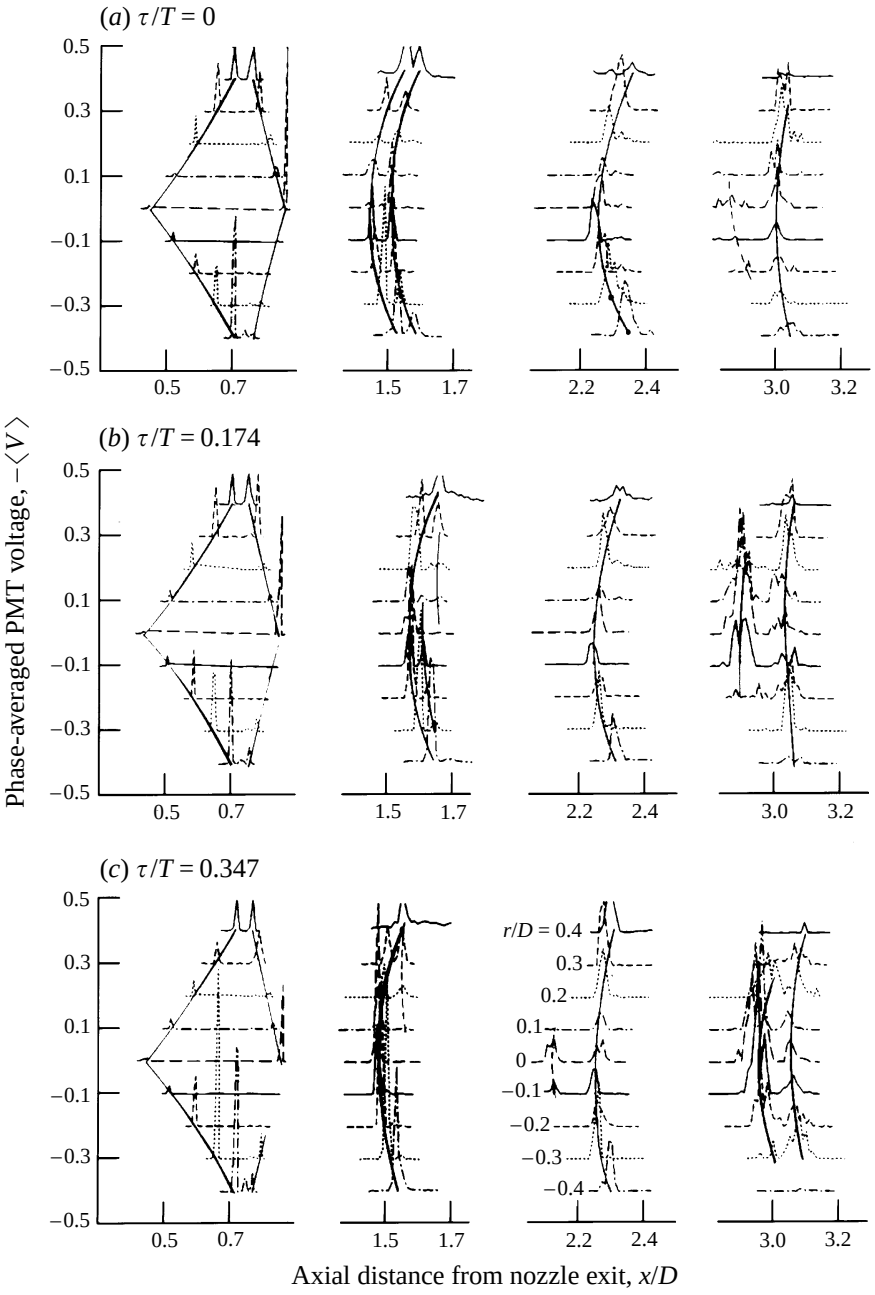

FIGURE 8 (*a–c*). For caption see facing page.

millimetre) than the following shocks, and this motion is not clearly detectable in this plot. The oscillation amplitude of the subsequent shocks progressively increases, and each shock also demonstrates the splitting behaviour as discussed earlier. Some indication of shock splitting is visible in the spark schlieren photographs of figure 2. The third shock is clearly split in figure 2(*b*), and has recombined in 2(*e*). A split second shock can be seen in figure 2(*d*). The ciné films of Westley & Wooley (1968*a*, 1970) also show a similar splitting process. Clearly, the passage of the coherent vortices is the

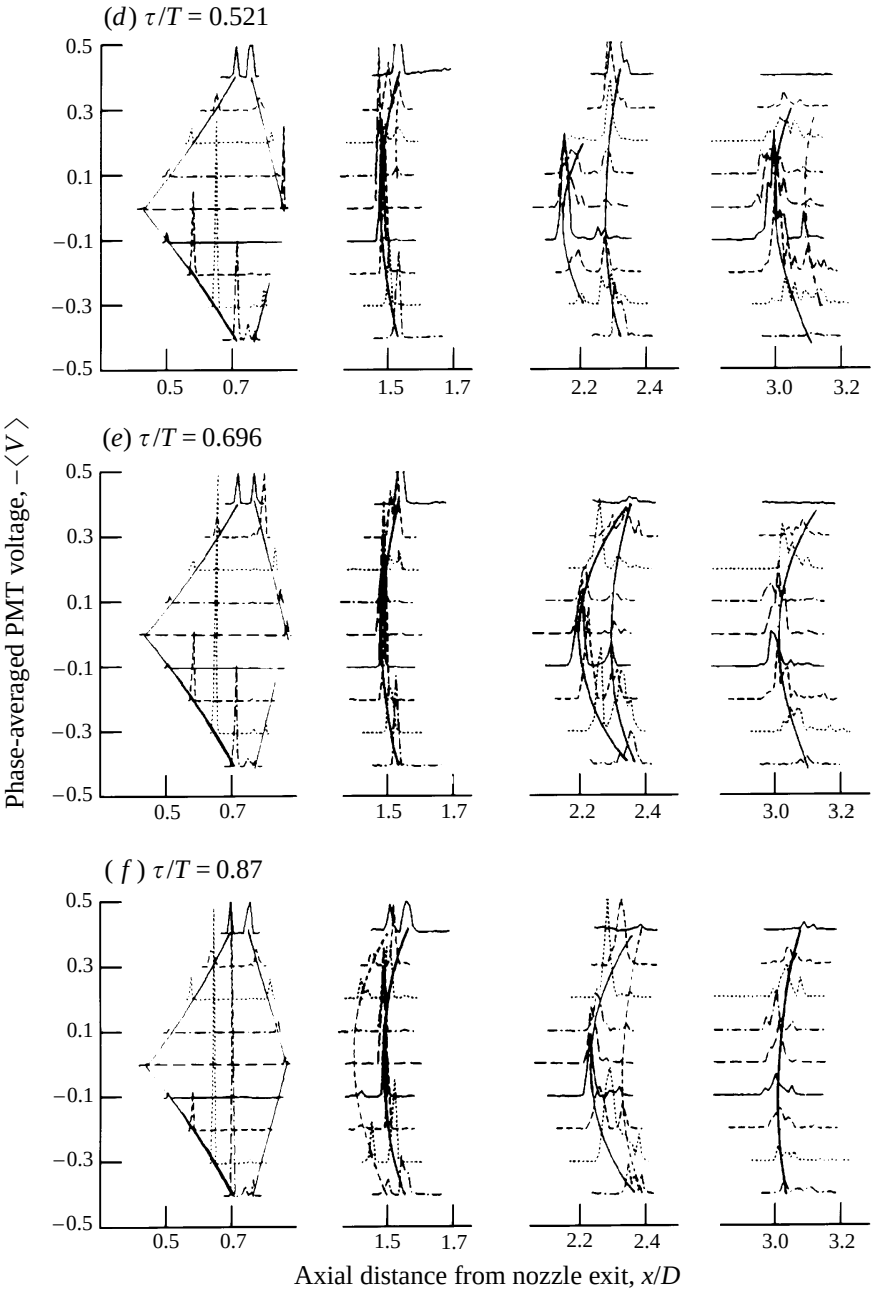

FIGURE 8. Phase-averaged PMT data obtained at nine different radial stations arranged to show the instantaneous profiles of first four shocks in $M_j = 119$ jet at the indicated phases of the screech cycle.

reason for this behaviour. A careful examination of the schlieren photographs shows that the splitting process occurs as a convected vortical structure spills over a shock disk. The eventual recombination occurs when the vortex moves to the middle of the following shock cell.

Returning to figure 8, the splitting process occurs at a progressively increasing phase of the screech cycle for a shock placed further downstream. The time difference

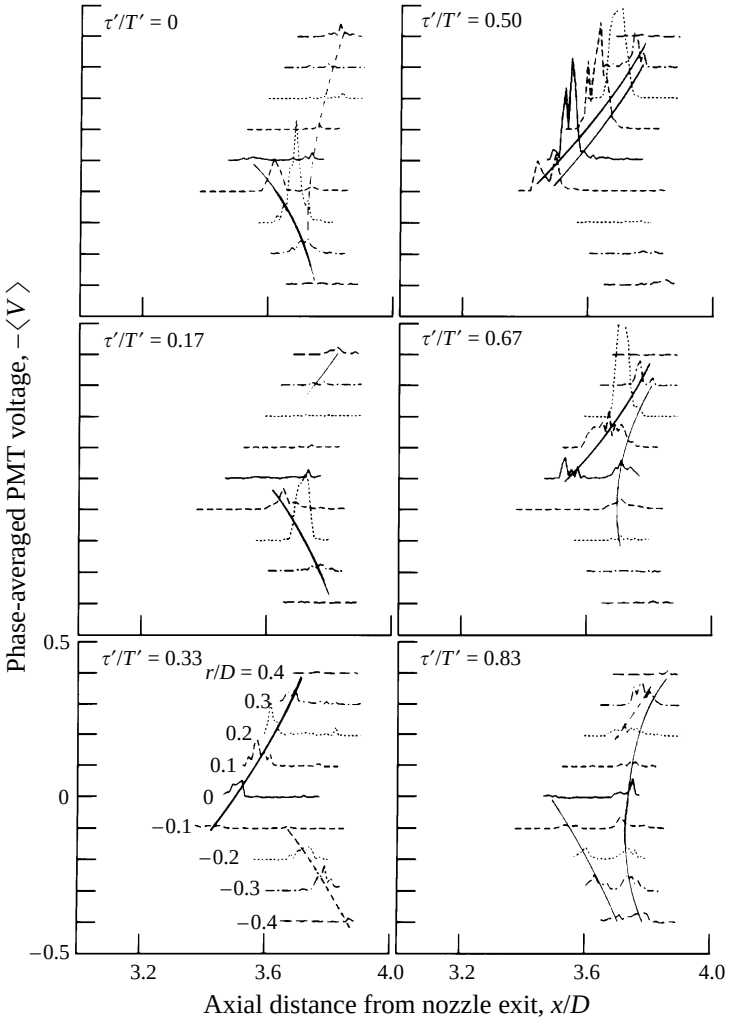

FIGURE 9. Phase-averaged PMT data obtained at nine different radial stations arranged to show the instantaneous profiles of the third shock in $M_j = 1.42$ jet at the indicated phases of the screech cycle.

$(\Delta\tau/T)_{meas}$ in the occurrence of splitting between the second and third, and the third and fourth shock is measured to be 0.62. This is nearly the same time (within experimental accuracy) needed for a vortical structure to move a shock cell distance L_s. The average convective velocity, u_c of the organized vortices in this jet is measured to be $238\ \mathrm{m\ s^{-1}}$ (Panda 1996) and the average shock cell spacing $L_s = 19.5$ mm. Therefore, the average time needed to move a shock cell distance, normalized by screech time period T, is

$$\left(\frac{\Delta\tau}{T}\right)_{est} = \frac{L_s}{u_c T} = 0.69.$$

The helical shock motion in the $M_j = 1.42$ jet is far more complicated than the axisymmetric motion presented above. The oscillation of the first shock is described earlier (figure 6). The profiles of the third shock at various phases of the screech cycle are presented in figure 9. This figure also demonstrates a splitting behaviour similar to that described earlier. However, the conspicuous aspect is the disappearance of either

M_j	Strouhal number screech mode SPL at lip	Average shock cell spacing, L_s/D	r/D	Amplitude of oscillation/D 1st shock	2nd shock	3rd shock	4th shock
1.19	0.59	0.77	0.0	0.025	0.12	0.19	0.29
	Axisymmetric		0.2	0.02	0.13	0.13	0.22
	149.5 dB		0.4	0.025	0.06	0.07	0.10
1.42	0.33	1.28	0.2	0.04	0.17	0.22	0.48
	Helical		0.4	0.04	0.084	0.08	
	160.6 dB						

TABLE 1. Measured amplitude of shock motion.

the upper ($r/D > 0$) or the lower ($r/D < 0$) half of the conical shock boundary during certain phases of the oscillation cycle. The upper half of the conical boundary is absent at $\tau'/T' = 0$ when the lower half is the strongest, while the lower half is absent at $\tau'/T' = 0.5$ when the upper half is the strongest. The flow visualization photograph of figure 3 also supports this measurement. The upper half of the second shock in figure 3(*a*) and the lower half of the same in figure 3(*c*) are nearly absent. There is a 180° phase difference between the above two figures. The third shock also shows similar behaviour. Nevertheless, it should be pointed out that any definite information on shock motion is difficult to obtain from a schlieren photograph. The dark regions of the jet, in a schlieren photograph, only represent a compression region which may or may not be bounded by a shock wave.

One effect of shock splitting is the large, spatial amplitude of motion that is more than one third of the average shock spacing. The amplitudes of shock motion, shown in Table 1, were obtained from the phase-averaged data plotted similar to figure 6(*a*). Table 1 also shows the screech amplitude at the nozzle lip. The oscillation amplitudes are expected to increase with an increase in the screech level. The Strouhal number is based on the screech frequency, fully expanded jet velocity, U_j, and the nozzle diameter. The large-amplitude shock motion, inside the potential core, is also responsible for a broadening of the r.m.s. voltage spikes mentioned earlier in conjunction with figure 4. Table 1 shows that the first shock oscillates with a nearly constant amplitude from the tip to the core; for all other shocks, the amplitude is minimum at the tip and maximum at the core. Oscillation amplitude also increases progressively for the shock formed further downstream. The shocks formed after the fourth one are very weak and highly distorted. The PMT signal also becomes weak and difficult to analyse. Such data are not presented in this paper.

4. Analytical formulation of shock oscillation based on the linear theory

In an underexpanded jet, shock cells are formed owing to the excess pressure (Δp) over the ambient level (P_a) present at the nozzle exit. The steady scenario is perturbed in a screeching jet by the presence of the screech tone that propagates along the jet boundary (Panda 1996). The pressure fluctuations associated with the screech sound effectively modulate the steady ambient level (figure 10). In the following analysis the oscillation of the jet column owing to the periodic oscillation of the ambient level is performed based on the linear theory of the shock cell structure. The steady state solution of shock cell structure was obtained by Pack (1950); the following analysis extends it to the unsteady situation. The success of the Pack solution is in predicting

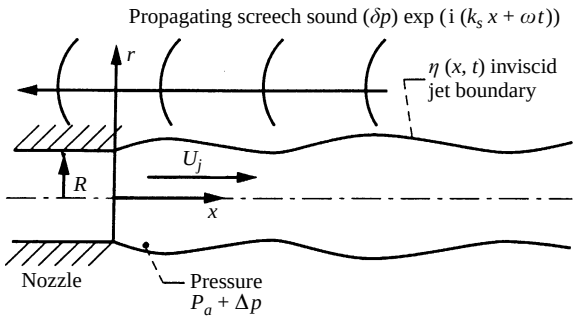

FIGURE 10. Schematic of a screeching, underexpanded jet column.

the shock locations, which are determined as the inflectional points in the boundary displacement. The goal of the present analysis is to calculate the oscillation of the inflectional points and thereby determine the amplitude of shock oscillation along the jet boundary. The analysis does not strive to predict the frequency and amplitude of screech tone; these are assumed to be known experimental data. The linear analysis is applicable to the first shock and perhaps justifiable to predict the small-oscillation amplitude of all others in the shear layer. The nonlinear mechanisms leading to the large-amplitude shock oscillation in the jet core are discussed in the next section. For the present vortex sheet analysis the shear layer around the jet is assumed to be thin and the dynamics of the shock oscillation is primarily believed to be an inviscid phenomenon.

The unsteady, linearized pressure perturbation equation that can be obtained from the linearized continuity, momentum and energy equation is given by (see Howe & Ffowcs Williams 1978):

$$\frac{1}{c_j^2}\left(\frac{\partial}{\partial t}+U_j\frac{\partial}{\partial x}\right)^2 p-\frac{\partial^2 p}{\partial x^2}-\frac{1}{r}\frac{\partial}{\partial r}\left(r\frac{\partial p}{\partial r}\right)=0, \tag{1}$$

where, c_j is the speed of sound in fully expanded jet, U_j is the fully expanded jet velocity, and p is the axisymmetric perturbation pressure at the nozzle exit. A solution of the steady part of equation (1) is known as the Prandtl–Pack solution (Pack 1950; Tam 1972; Howe & Ffowcs Williams 1978). For the present unsteady formulation, the effective excess pressure over the ambient level along the jet boundary is a sum of the steady part (Δp) and the propagating part associated with screech sounds. Since pressure is reckoned relative to the steady ambient level, the boundary conditions that equation (1) must satisfy are:

$$\left.\begin{array}{ll} p=-\Delta p-(\delta p)\exp\left(\mathrm{i}(k_s x+\omega t)\right) & (r=R,\quad x>0),\\ p=0 & (x<0). \end{array}\right\} \tag{2}$$

where, R is the jet radius, ω and k_s are the screech frequency and wavenumber, respectively, and δp is the amplitude of pressure fluctuation in the screech tone. The radial displacement of the jet boundary, $\eta(x,t)$ (sketched in figure 10), from $r=R$ is obtained from the radial component of the momentum equation as:

$$\left(\frac{\partial}{\partial t}+U_j\frac{\partial}{\partial x}\right)^2\eta=-\frac{1}{\rho_j}\frac{\partial p}{\partial r}. \tag{3}$$

Since, the pressure fluctuations associated with the screech tone are far smaller than

the steady part of the excess pressure, $\delta p \quad \Delta p$, a separated form of the solution is looked for:

$$p(r, x, t) = p_1(r, x) + p_2(r, x)\, e^{i\omega t}.$$

This is permissible owing to the linearity of the governing differential equation. The two parts of the perturbation pressure, p_1 and p_2, satisfy, respectively, the steady and unsteady part of the boundary conditions. In a similar fashion the boundary displacement $\eta(x, t)$ is also separated into a steady and a time-dependent part

$$\eta(x, t) = \eta_1(x) + \eta_2(x)\, e^{i\omega t}. \tag{4}$$

Now the governing equation (1) and the boundary conditions (2) and (3) can be separated out into a steady and a time-dependent part. First, the steady state equation and boundary conditions are as follows:

$$(M_j^2 - 1)\frac{\partial^2 p_1}{\partial x^2} - \frac{1}{r}\frac{\partial p_1}{\partial r} - \frac{\partial^2 p_1}{\partial r^2} = 0, \tag{5a}$$

$$\left.\begin{aligned} p_1 &= -\Delta p \quad (r = R, \quad x > 0), \\ p_1 &= 0 \qquad (x < 0), \end{aligned}\right\} \tag{5b}$$

$$U_j^2 \frac{d^2 \eta_1}{dx^2} = -\frac{1}{\rho_j}\frac{\partial p_1}{\partial r}. \tag{5c}$$

where, $M_j = U_j / c_j$. The unsteady parts are separated out as:

$$-(M_j^2 - 1)\frac{\partial^2 p_2}{\partial x^2} - 2iM_j \frac{\omega}{c_j}\frac{\partial p_2}{\partial x} + \frac{\omega^2}{c_j^2} p_2 + \frac{1}{r}\frac{\partial p_2}{\partial r} + \frac{\partial^2 p_2}{\partial r^2} = 0, \tag{6a}$$

$$\left.\begin{aligned} p_2 &= -(\delta p)\exp(ik_s x) \quad (r = R, \quad x > 0), \\ p_2 &= 0 \qquad\qquad\qquad\quad (x < 0), \end{aligned}\right\} \tag{6b}$$

$$-\omega^2 \eta_2 + 2iU_j \omega \frac{d\eta_2}{dx} + U_j^2 \frac{d^2 \eta_2}{dx^2} = -\frac{1}{\rho_j}\frac{\partial p_2}{\partial r}. \tag{6c}$$

The steady part in equations 5(*a–c*) has been solved in the past, as referred to earlier. The solution following Howe & Ffowcs Williams (1978) is as follows:

$$\eta_1 = \frac{(\Delta p)\beta^2 R}{\rho_j U_j^2}\left[\frac{1}{2} - 2\sum_{n=1}^{\infty}\frac{1}{\lambda_n^2}\cos\left(\frac{\lambda_n x}{\beta R}\right)\right]. \tag{7}$$

where, $\beta = (M_j^2 - 1)^{1/2}$ and λ_n is the nth positive root of the zeroth order Bessel function J_0.

For a solution of the time-dependent part, the Fourier x-transform pairs of pressure p_2 and boundary displacement component η_2 are introduced:

$$\left.\begin{aligned} \overline{p_2}(r, k_2) &= \frac{1}{2\pi}\int_{-\infty}^{\infty} p_2(r, x)\exp(-ik_2 x)\, dx, \\ p_2(r, x) &= \int_{-\infty}^{\infty} \overline{p_2}(r, k_2)\exp(ik_2 x)\, dk_2, \end{aligned}\right\} \tag{8a}$$

$$\left.\begin{aligned} \overline{\eta_2}(r, k_2) &= \frac{1}{2\pi}\int_{-\infty}^{\infty} \eta_2(r, x)\exp(-ik_2 x)\, dx, \\ \eta_2(r, x) &= \int_{-\infty}^{\infty} \overline{\eta_2}(r, k_2)\exp(ik_2 x)\, dk_2. \end{aligned}\right\} \tag{8b}$$

The transforms of equation (6*a*) and the boundary conditions (6*b*) produce:

$$\frac{\partial^2\overline{p_2}}{\partial r^2}+\frac{1}{r}\frac{\partial\overline{p_2}}{\partial r}+B^2\overline{p_2}=0 \quad \text{where} \quad B^2=k_2^2(M_j^2-1)+2k_2M_j\frac{\omega}{c_j}+\frac{\omega^2}{c_j^2}, \tag{9a}$$

and

$$\overline{p_2}=-\frac{\delta p}{2\pi\mathrm{i}(k_2-k_s)}. \tag{9b}$$

The solution of equation (9*a*) that remains bounded at $r=0$ is $\overline{p_2}=A(k_2)\,J_0(Br)$. The constant A is evaluated using boundary condition (9*b*); this leads to:

$$\overline{p_2}=-\frac{\delta p}{2\pi\mathrm{i}}\frac{J_0(Br)}{(k_2-k_s)\,J_0(BR)}. \tag{10}$$

The final goal of the analysis is to determine the unsteadiness of the jet boundary (η). The unsteady part of the boundary displacement (η_2) satisfies equation 6(*c*). A Fourier transform of this equation produces:

$$(\omega+k_2U_j)^2\overline{\eta_2}=\frac{1}{\rho_j}\frac{\partial\overline{p_2}}{\partial r}.$$

A substitution of $\overline{p_2}$ by equation (10) and an inverse transform provides an integral relation as follows:

$$\eta_2=\frac{(\delta p)}{2\pi\mathrm{i}\rho_j}\int_{-\infty}^{\infty}\frac{B}{(k_2-k_s)(\omega+k_2U_j)^2}\frac{J_1(BR)}{J_0(BR)}\exp(\mathrm{i}k_2x)\,\mathrm{d}k_2. \tag{11}$$

The integrand has a second-order pole at $k_2=-\omega/U_j$, a simple pole at $k_2=k_s$, and a set of simple poles at $BR=\pm\lambda_n(1\leqslant\lambda_n\leqslant\infty)$. The integrand is determined by residues. Note that to evaluate residues for the last set of poles, a quadratic equation is encountered, as is evident from equation (9*a*):

$$k_2^2(M_j^2-1)+2M_jk_2\frac{\omega}{c_j}+\left(\frac{\omega}{c_j}\right)^2-\left(\frac{\lambda_n}{R}\right)^2=0.$$

The roots of the above equation are at:

$$k_2=Q_n^+,Q_n^-=\frac{-M_jS'\pm(\lambda_n^2(M_j^2-1)+S'^2)^{1/2}}{R(M_j^2-1)} \qquad \left(S'=\frac{\omega R}{c_j}\right). \tag{12}$$

Therefore, the residues have to be evaluated in the limits of $k_2\to Q_n^+$ and $k_2\to Q_n^-$.

In the final solution, the steady and the time-dependent contributions are summed up according to equation (4). The real part is of physical interest:

$$\begin{aligned}\eta=\eta_1+\eta_2=&\frac{(\Delta P)\beta^2R}{\rho_jU_j^2}\left[\frac{1}{2}-2\sum_{n=1}^{\infty}\frac{1}{\lambda_n^2}\cos\left(\frac{\lambda_nx}{\beta R}\right)\right]\\&+\frac{\delta p}{\rho_j}\left[\frac{B_sJ_1(B_sR)}{(\omega+k_sU_j)^2J_0(B_sR)}\cos(k_sx)\right.\\&+\frac{F}{U_j(\omega+U_jk_s)}\left\{\left(SF-2+\frac{\omega}{\omega+U_jk_s}\right)\cos\left(\frac{\omega x}{U_j}\right)+\left(\frac{\omega x}{U_j}\right)\sin\left(\frac{\omega x}{U_j}\right)\right\}\\&\left.+\frac{2}{R^2}\sum_{n=1}^{\infty}\frac{\lambda_n^2}{(\lambda_n^2\beta^2+S'^2)^{1/2}}\left\{-\frac{\exp(\mathrm{i}Q_n^+x)}{(\omega+Q_n^+U_j)^2(Q_n^+-k_s)}+\frac{\exp(\mathrm{i}Q_n^-x)}{(\omega+Q_n^-U_j)^2(Q_n^--k_s)}\right\}\right]\exp(\mathrm{i}\omega t),\end{aligned} \tag{13}$$

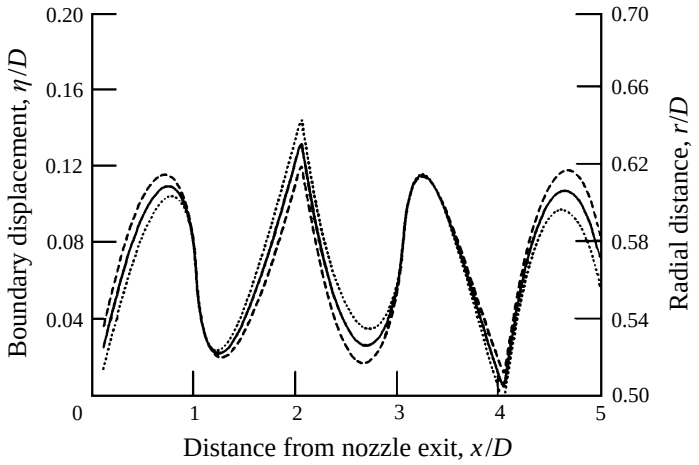

FIGURE 11. Calculated boundary displacement function for $M_j = 1.42$ jet; ——, steady state part; – – –, complete unsteady solution for $\omega t = 0$; · · ·, $\omega t = \pi$.

where

$$S = \frac{\omega R}{U_j},$$

$$B_s = \left(k_s^2 \beta^2 + 2k_s M_j \frac{\omega}{c_j} + \frac{\omega^2}{c_j^2}\right)^{1/2},$$

$$F = \frac{I_1(S)}{I_0(S)} \quad (I_1, I_0 = \text{modified Bessel functions of 1st and zeroth order}).$$

The right-hand side of the first line of equation (13) represents the steady state displacement of the jet boundary. The following three lines show three parts of the time-dependent component. The first part (2nd line of equation (13)) shows a disturbance at the same wavenumber of the forcing acoustic waves; the second part (3rd line) is a spatially growing disturbance with a new wavenumber of ω/U_j, and the third part (4th line) shows two sets of waves of wavenumbers Q_n^+ and Q_n^-. From the third part Q_1^+ is the principal contributor towards the total sum. For a numerical calculation the excess pressure above the ambient level, Δp, can be determined from M_j and the plenum pressure p_0 using isentropic relations:

$$\Delta p = p_0[-(1 + \tfrac{1}{2}(\gamma - 1) M_j^2)^{-\gamma/(\gamma-1)} + \tfrac{1}{2}(\gamma + 1)^{-\gamma/(\gamma-1)}],$$

where, γ is the ratio of specific heats. The amplitude of the screech tone is measured at the nozzle lip and the amplitude of pressure fluctuation is determined from the measured sound pressure level (SPL) data:

$$\delta p = 2\sqrt{2}\, 10^{(\mathrm{SPL}/20 - 5)}.$$

The algebraic boundary displacement relation of equation (13) was evaluated for the $M_j = 1.42$ jet at two different phases of the screech cycle. The unsteady displacement function, η, at two different phases ($\omega t = 0$ and π) as well as the steady state component, η_1, are shown in figure 11. As expected, the fluctuation amplitude is small. From the steady state analysis (Pack 1950), it is known that the shock locations (at $r = R$) are the local minima in the boundary displacement function. By closely examining figure 11, it is found that the minima locations change by a small amount

M_j	Screech frequency	SPL at nozzle lip (dB)	Shock number from nozzle exit	Oscillation amplitude/jet diameter	
				Calculated	Measured
1.186	8425	149.5	1	0.0205	0.022
			2	0.075	0.06
1.242	5500	158.7	1	0.0525	0.033
1.424	5375	160.6	1	0.0525	0.036
			2	0.1022	0.084
1.52	4875	160.2	1	0.065	0.045
1.58	4650	158.5	1	0.05	0.05

TABLE 2. Comparison between calculated and measured shock oscillation amplitudes at jet boundary.

at various phases (ωt) of the screech cycle. Equation (13) shows that the spatial and temporal dependency of the unsteady part are separable. Therefore, the shock oscillation amplitude can be calculated from the separation of the minima at $\omega t = 0$ and $\omega t = \pi$. Table 2 gives the calculated and measured amplitudes for the first and the second shocks at various jet operating conditions. The shock motion is measured at $r/D = 0.45$. The sound pressure amplitudes, measured at the nozzle lip using a microphone, are also tabulated. There is a reasonable agreement between the measured and the calculated shock oscillation amplitudes, especially considering the large uncertainty in the measured data (estimated to be $\pm 15\%$) and the limitations of the analysis. The measurement uncertainty is due to the finite diameter of the laser beam and the plenum pressure fluctuation. The present axisymmetric analysis is valid only for a similar screech mode, yet data presented in table 2 include flapping and helical modes.

A side benefit of the above analysis is an insight into the receptivity of the jet column from the external acoustic pressure fluctuations. In a screeching jet, excitation of the shear layer fluctuations by the screech tone sustains the feedback loop. The current belief is that the receptivity process occurs at the nozzle lip (Powell 1953; Tam 1991). The present analysis demonstrate a different route, where the acoustic fluctuations are shown to generate various waves along the jet boundary without the necessity of the nozzle lip.

5. Additional causes of shock oscillation

The periodic pressure perturbation from passing sound waves is one of the many causes for shock oscillation. It is the major reason for the oscillation of the first shock. It is conjectured that three additional factors come into play for all others shocks lying further downstream. First, the coupling between the motion of each shock; secondly, the pressure fluctuations associated with the passage of the large organized structure along the jet shear layer, and thirdly, the distortion of the supersonic–subsonic interface in the jet shear layer caused by the same organized vortices. The first factor arises as the flow oscillation created by a moving shock is transmitted to the following ones. Since, the flow field downstream of an oblique shock remains supersonic, information on shock oscillation does not propagate upstream, at least not through the potential core. Therefore, the first shock is expected to remain uncoupled from that of the following ones. The coupling factor will be progressively pronounced for shocks formed further downstream.

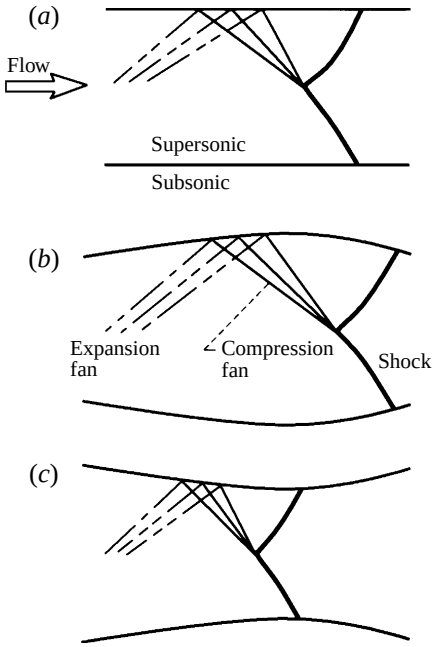

FIGURE 12. Schematic of shock movement caused by distortions in the supersonic–subsonic interface; (*a*) undistorted, (*b*) bulged out interface, (*c*) bulged in interface.

Perhaps, a combination of the second and third factors is the primary reason for the large-amplitude shock oscillation and the associated shock-splitting phenomenon. In an underexpanded jet, shocks are formed by a mechanism of internal reflection of expansion waves into compression waves from the supersonic–subsonic interface, and the subsequent coalescence of the compression waves (Pack 1948). The passage of the large turbulent structures is expected to distort this interface. For example, let us consider the $M_j = 1.19$ jet for which the organized structures are in the axisymmetric mode. The passage of such structures will cause the otherwise cylindrical interface to bulge outward and inward periodically (figure 12). In the former situation, the shock will be formed at a downstream location and, for the latter at an upstream location. The amplitude of shock oscillation, governed by the above scenario, will progressively increase as the organized structures grow in size. This is, once again, consistent with the experimental observation that the shocks formed further downstream oscillate by a large amplitude.

Aside from the large-oscillation amplitude a significant perturbation in the supersonic–subsonic interface is expected to change the focusing of the compression wave, which may not coalesce sufficiently to form a shock. This, perhaps, is the reason for the periodic appearance and disappearance of the alternate sides of the shock cone in the $M_j = 1.42$ jet (figure 9).

6. Summary and conclusion

The oscillatory motion of various shocks formed in moderately underexpanded jets ($M_j = 1.19$ and 1.42) issuing from a convergent nozzle is studied in this paper. At these operating conditions the jets produce intense screech tones in, respectively, axisymmetric and helical modes. The various reasons for shock oscillation are also discussed in this paper. The primary results are as follows.

1. A new optical detection technique, based on the laser light scattering by shock waves, is used to determine instantaneous shock position. By relating the time and position information to the phase of the screech cycle, a vast amount of information on the amplitude, phase, and nonlinearity of the shock motion is gathered. It is determined that all but the first shock move by a small amplitude at the tip and by a very large amplitude at the core. Since the motion is caused by periodic vortices passing through the shear layer, the part of the shock lying in the shear layer is expected to move the most. The analysis of shock–turbulence interaction by Ribner (1969), and the numerical simulations of a two-dimensional vortex interacting with a single shock (Ellzey *et al*. 1995) also demonstrate that the region of direct interaction is the region of the largest shock deformation. The experimental data clearly differ from these results. The discrepancies are due to some major factors, such as the boundedness of each shock by a shear layer and the modifications of the shock formation mechanisms by the passing vortices, that are not considered in the simple models.

2. The instantaneous profiles of the first four shocks over an oscillation cycle were constructed through detailed phase-averaged measurements. Such data show a splitting of each shock (except for the first one) into two weaker ones. During a cycle of motion the downstream shock progressively fades away while a new shock appears upstream. This 'moving staircase-like' motion results in the significantly large-oscillation amplitude of all but the first shock. The first shock demonstrates a smooth sinusoidal motion about its mean positions.

3. The time-averaged axial velocity data obtained by laser Doppler velocimetry show a periodic variation where any discontinuity is smoothed by shock oscillation. Shock oscillation is further confirmed by the appearance of bimodal particle velocity histograms at the shock locations.

4. There is more than one reason for shock oscillation. One interesting factor, special to a screeching jet, is the influence of the intense screech tone that propagates upstream along the jet boundary. The screech tone adds a small fluctuating component to the steady ambient pressure. The resulting periodic oscillation of the jet boundary is determined through an analytical solution of the unsteady, linearized Euler's equation. The final solution shows the generation of three types of waves, all of which have the same frequency as that of the screech sound, but different wavenumbers. One of them is found to grow along the jet flow direction. The net effect of all such waves in oscillating the first and the second shock is calculated, and the oscillation amplitude is compared with the measured value for various jet operating conditions. A reasonable agreement between the two shows the usefulness of the analysis.

5. Spark schlieren photographs demonstrate that a periodic convection of large organized vortices over the shock train results in the shock-splitting and the large-oscillation amplitude of all but the first shock. The nonlinear mechanisms go beyond the scope of the linearized analysis. However, the effect of the organized vortices in changing the shock formation mechanism by modifying the sonic line is qualitatively discussed in the text.

The author wishes to acknowledge numerous suggestions and helpful discussions with Dr K. B. M. Q. Zaman of NASA Lewis Research Center during the course of the experimental work. The insightful comments by Professor Kevin Kreider, Department of Mathematical Sciences, University of Akron, on the analytical modelling are also acknowledged.

REFERENCES

Cain, A. B., Bower, W. W., Walker, S. H. & Lockwood, M. K. 1995 Modeling supersonic jet screech. Part 1. Vortical instability wave modeling. *AIAA Paper* 95-0506.

Chriss, R. M. 1991 A laser velocimeter investigation of the normal shock-wave boundary layer interaction. *NASA Tech. Memo.* 105201.

Davis, M. G. & Oldfield, D. E. S. 1962 Tones from a chocked axisymmetric jet. I. Cell structure, eddy velocity and source locations. *Acustica* **12** (4), 257–277.

Ellzey, J. L., Henneke, M. R., Picone, J. M. & Oran, E. S. 1995 The interaction of a shock with a vortex: Shock distortion and production of acoustic waves. *Phys. Fluids* **7**, 172–184.

Harper-Bourne, M. & Fisher, M. J. 1974 The noise from shock waves in supersonic jets. *AGARD* CP131, *Noise Mechanism.*

Hay, J. A. & Rose, E. G. 1970 In flight shock cell noise. *J. Sound Vib.* **11**, 411–420.

Howe, M. S. & Ffowcs Williams, J. E. 1978 On the noise generated by an imperfectly expanded supersonic jet. *Phil. Trans. R. Soc. Lond.* A **289**, 271–314.

Johannesen, N. H. 1957 The mixing of free axially-symmetric jets of Mach number 1.40. *ARC R & M* 3291.

Johannesen, N. H. & Meyer, R. E. 1950 Axially-symmetric supersonic flow near the center of an expansion. *Aero. Q.* **2**, 127–142.

Lassiter, L. W. & Hubbard, H. H. 1954 The near noise field of static jets and some model studies of devices for noise reduction. *NACA Tech. Note* 3187.

Love, E. S., Eugene, S., Lee, L. P. & Woodling, M. J. 1959 Experimental and theoretical studies of axisymmetric free jets. *NASA Tech. Rep.* R-6.

Meadows, K. & Caughey, D. 1996 The roles of shock motion and deformation in the generation of shock noise. *AIAA Paper* 96-1777.

Morris, P. J., Bhat, T. R. S. & Chen, G. 1989 A linear shock cell model for jets of arbitrary exit geometry. *J. Sound Vib.* **132**, 199–211.

Pack, D. C. 1948 On the formation of shock-waves in supersonic gas jets (two-dimensional flow). *Q. J. Mech. Appl. Maths* **1**, 451–469.

Pack, D. C. 1950 A note on Prandtl's formula for the wave-length of a supersonic gas jet. *Q. J. Mech. Appl. Maths* **3**, 173–181.

Panda, J. 1995*a* Wide angle light scattering in shock-laser interaction. *AIAA J.* **33**, 2429–2431.

Panda, J. 1995*b* A shock detection technique based on light scattering by shock. *AIAA J.* **33**, 2431–2433.

Panda, J. 1996 An experimental investigation of screech noise generation. *AIAA Paper* 96-1718, also submitted for publication in *J. Fluid Mech.*

Panda, J. & Adamovsky, G. 1995 Laser light scattering by shock waves. *Phys. Fluids* **7**, 2271–2279.

Powell, A. 1953 On the mechanism of choked jet noise. *Proc. Phys. Soc. Lond.* **66**, 1039–1056.

Ribner, H. S. 1969 Acoustic energy flux from shock-turbulence interactions. *J. Fluid Mech.* **35**, 299–310.

Seiner, J. M. 1984 Advances in high speed jet aeroacoustics. *AIAA Paper* 84-2275.

Seiner, J. M., Manning, J. C. & Ponton, M. K. 1987 Model and full scale study of twin supersonic plume resonance. *AIAA Paper* 87-0244.

Tam, C. K. W. 1972 On the noise of a nearly ideally expanded supersonic jet. *J. Fluid Mech.* **51**, 69–95.

Tam, C. K. W. 1988 The shock-cell structures and screech tone frequencies of rectangular and non-axisymmetric supersonic jets. *J. Sound Vib.* **121**, 135–147.

Tam, C. K. W. 1991 Jet noise generated by large-scale coherent motion. In *Aeroacoustics of Flight Vehicles: Theory and Practice*, *vol. 1: Noise Sources* (ed. H. H. Hubbard), pp. 311–390. NASA RP-1258, WRDC TR-90-3052.

Tam, C. K. W. & Jackson, J. A. 1985 A multiple-scales model of the shock-cell structure of imperfectly expanded supersonic jets. *J. Fluid Mech.* **153**, 123–149.

Vom Stein, H. D. & Pfeifer, H. J. 1972 Investigation of the velocity relaxation of micron-sized particles in shock waves using laser radiation. *Appl. Optics* **11** (2).

Westley R. & Woolley, J. H. 1968*a* *Flow and Sound Visualization of an Axisymmetric Choked Jet*. 16 mm Ciné Film, no. 13 (1968), NRC/NAE library.

Westley R. & Woolley, J. H. 1968*b* An investigation of the near noise fields of a choked axisymmetric air jet. *Aerodynamic Noise*, pp. 147–167. University of Toronto Press.

Westley, R. & Woolley, J. H. 1970 *Flow and Sound Visualization of an Axisymmetric Choked Jet*. 16 mm Ciné Film, no. 20 (1970), NRC/NAE library.

Yanta, W. J., Gates, D. F. & Brown, F. W. 1971 The use of a laser doppler velocimeter in supersonic flow. *AIAA Paper* 71-287.